Analytical model and stability analysis of the leading edge spar of a passively morphing ornithopter wing

Bioinspiration & Biomimetics

RECEIVED
13 February 2015

REVISED
12 August 2015

ACCEPTED FOR PUBLICATION
10 September 2015

PUBLISHED
26 October 2015

PAPER

Analytical model and stability analysis of the leading edge spar of a passively morphing ornithopter wing

Aimy Wissa[1], Joseph Calogero[2], Norman Wereley[3], James E Hubbard jr[4] and Mary Frecker[3]

[1] University of Illinois at Urbana Champaign, 1206 West Green Street, Urbana, IL 61801, USA
[2] Pennsylvania State University, 314D Leonhard Building, University Park, PA 18602, USA
[3] University of Maryland, 3179 Glenn L. Martin Hall Bldg, College Park, MD 20742, USA
[4] University of Maryland, 100 Exploration Way, Hampton, VA 23666, USA

E-mail: awissa@illinois.edu

Keywords: ornithopter, stability analysis, linear time periodic model, Mathieu's equation

Abstract

This paper presents the stability analysis of the leading edge spar of a flapping wing unmanned air vehicle with a compliant spine inserted in it. The compliant spine is a mechanism that was designed to be flexible during the upstroke and stiff during the downstroke. Inserting a variable stiffness mechanism into the leading edge spar affects its structural stability. The model for the spar–spine system was formulated in terms of the well-known Mathieu's equation, in which the compliant spine was modeled as a torsional spring with a sinusoidal stiffness function. Experimental data was used to validate the model and results show agreement within 11%. The structural stability of the leading edge spar–spine system was determined analytically and graphically using a phase plane plot and Strutt diagrams. Lastly, a torsional viscous damper was added to the leading edge spar–spine model to investigate the effect of damping on stability. Results show that for the un-damped case, the leading edge spar–spine response was stable and bounded; however, there were areas of instability that appear for a range of spine upstroke and downstroke stiffnesses. Results also show that there exist a damping ratio between 0.2 and 0.5, for which the leading edge spar–spine system was stable for all values of spine upstroke and downstroke stiffnesses.

Nomenclature

I_1	mass moment of inertia for the inboard rod (kg m^2)	k_T	stiffness of the torsional spring representing the compliant spine (N m rad^{-1})
I_2	mass moment of inertia for the outboard rod (kg m^2)	k_d	compliant spine downstroke torsional stiffness (N m rad^{-1})
L_1	length of the inboard rod (m)	k_u	compliant spine upstroke torsional stiffness (N mrad^{-1})
L_2	length of the outboard rod (m)	m_1	mass of the inboard rod (Kg)
L_{spine}	length of the compliant spine (m)	m_2	mass of the outboard rod (Kg)
M	motor torque (N m)	N	number of data points used over one flapping cycle
T	flapping period (s)	t	time (s)
Y_{SR}	vertical displacement of the spine root marker (m)	$x_{2c.m.}$	horizontal displacement of the center of mass of the outboard rod (m)
Y_{ST}	vertical displacement of the spine tip marker (m)	$y_{2c.m.}$	vertical displacement of the center of mass of the outboard rod (m)
Y_{WR}	vertical displacement of the wing root marker (m)	θ_1	wing root angle (rad)
C_T	torsional damping coefficient (N m s rad^{-1})		

$\theta_{1\text{exp}}$	experimentally measured wing root angle (rad)
θ_2	spine root angle (rad)
$\theta_{2\text{exp}}$	experimentally measured spine root angle (rad)
ζ	non-dimensional damping ratio
φ	wing stroke angle (rad)
ω	flapping frequency (rad s^{-1})
$\ddot{\cdot}$	second derivative with respect to time

1. Introduction

During the last few decades, flapping wing unmanned aerial vehicles (UAVs), or ornithopters, have shown the potential for advancing UAV performance in both the civil and military sectors [1]. An ornithopter is unique in that it can combine the agility and maneuverability of rotary wing aircraft with excellent performance in low Reynolds number flight regimes. These traits could yield improved performance over multiple mission scenarios. Nature achieves such performance in birds using wing gaits that are optimized for a particular flight condition [2–4]. The continuous vortex gait (CVG) is the desired bio-inspired kinematics to be implemented on a test ornithopter to improve steady level flight. A detailed discussion of the kinematics of the CVG can be found in [3]. The advantage of using the CVG is that it is an avian gait that can be implemented *passively* and requires motion in only one major joint, namely the wrist. The desired bending kinematics of the CVG can be achieved by inserting a contact-aided compliant mechanism called a compliant spine into the wing leading edge spar.

The compliant spine is designed to be flexible during the upstroke, while remaining stiff during the downstroke. Figure 1 shows a compliant spine design with three compliant joints. The design is flexible in bending during the upstroke because of the semi-circular compliant hinges, and it is stiff in bending during downstroke because the slanted faces come into contact with one another. References [5] and [6] detail the design and optimization of the compliant spine. Figure 2 illustrates the bending stiffness of one of the compliant spine designs when it is inserted in the spar. In the figure, the *Y*-axis represents the bending moment applied to the leading edge spar of the ornithopter with a compliant spine integrated in it. The *X*-axis represents the compliant spine tip bending angle. As illustrated, the desired stiffness of the compliant spine is stiff in the downstroke, similar to that of a rigid spar, and flexible in the upstroke.

The stiffness of the compliant spine is time varying. Inserting a variable stiffness compliant spine into the wing leading edge spar of a test ornithopter results in a parametrically excited system. A parametrically excited system is defined as a system in which one or more of the constitutive parameters of the problems, such as the stiffness, are varying with time [7]. Parametric excitations take the form of time varying coefficients in a system's equations of motion (EOM). The oscillations of parametrically excited systems are unlike the oscillations of free and forced systems where all the parameters are time invariant [8]. Unlike linear time invariant systems, areas of instability can arise in linear time variant systems even if the systems' EOMs are unforced and un-damped. Therefore, a stability analysis is essential for the leading edge spar–spine system to ensure the structural stability of the spar during testing. The leading edge spar–spine system is defined as the test ornithopter leading edge spar with a compliant spine design inserted at 37% of the wing half span, as shown in figure 3. Figure 4 shows the research platform considered here and table 1 includes the platform specifications [9].

Several work in the literature have considered the stability of flapping wing unmanned air vehicle both at the insect and avian scales, as well as in hover and forward flight. Orlowski and Girard presents an extensive review of the various analysis approaches of flight dynamics, stability and control of flapping wing air vehicles [10]. Also due to the time-varying inertial properties of flapping wing flight, several authors have applied Floquet's theory to determine the stability of the vehicle and account for the varying inertial effects [11–13]. Among this work, only one, to the best of the author's knowledge, transformed the EOM of a flapping wing in terms of Mathieu's equation and determined the stability in terms of a Strutt diagram [14]. This paper investigates the effect of the time varying stiffness rather than inertia. Moreover it uses both analytical and graphical methods such as the phase plane and Strutt diagrams to determine the stability of a flapping wing leading edge spar.

The remainder of this paper is organized as follows: section 2 formulates the leading edge spar–spine model and validates the model using experimental data and section 3 presents the stability analysis of the leading edge spar–spine system through transforming the EOM in terms of Mathieu's equation and using both an un-damped and damped model. The paper concludes with a summary of the modeling results.

2. Leading edge spar model

2.1. Leading edge spar EOM

The wing leading edge spar–spine system was modeled as two rigid rods connected by a torsional spring. Figure 5 shows the model of the leading edge spar–spine system along with the assumed boundary conditions. The torsional spring in this model was used to represent the compliant spine. One rod was inboard (closer to the wing root) of the compliant spine and the other was outboard of the compliant spine. The inboard rod had a pinned boundary condition at the

Figure 1. The compliant spine is designed to be stiff during the downstroke and flexible during the upstroke.

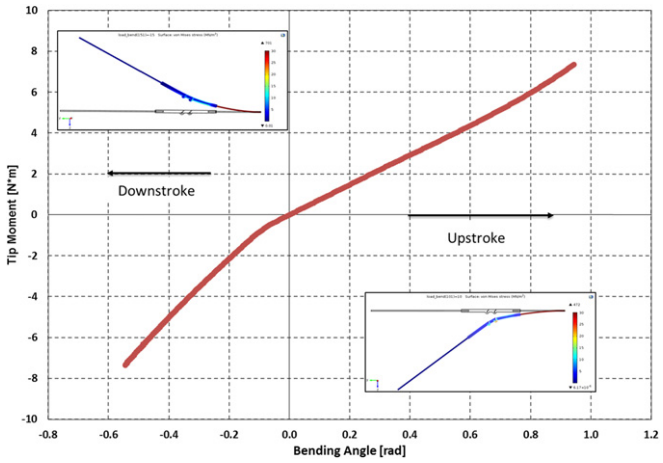

Figure 2. The applied bending moment versus bending angle of the spar–spine system. The plot shows that spar–spine system is stiff during the downstroke and flexible during the upstroke. The inset images show the von-mises stresses and bending deflections of the spar–spine system during the downstroke (left) and upstroke (right).

wing root and was connected to the torsional spring on its other end. The outboard rod had a free boundary condition at the wing tip and was connected to the torsional spring on its other end. Due to the periodicity of the flapping motion of the test ornithopter during free flight, the stiffness of the torsional spring representing the compliant spine was assumed to be linear time periodic and was described as:

$$k_T = \left(k_a + k_b\right) - k_b \cos\left(\frac{2\pi t}{T}\right) \quad (1)$$

where

$$k_a = k_u \quad (2)$$

$$k_b = \frac{k_d - k_u}{2}. \quad (3)$$

A sinusoidal function for the spring stiffness was chosen based on observations made during previous experiments [15]. The experimental deflections of the leading edge spar–spine system during the up and down strokes suggested a sinusoidal rather than a square wave or impulse stiffness function.

In equations 1 through 3 above, k_u and k_d are the upstroke and downstroke torsional stiffness of the compliant spine, t is time, and T is the period of one wing beat cycle. The values of k_u and k_d were determined based on the compliant spine design choice.

Figure 6 shows a schematic of the leading edge spar–spine system. In the figure, θ_1 is the wing root angle, θ_2 is the spine root angle. L_1 and m_1 are the length and mass of the inboard rod, L_2 and m_2 are the length and mass of the outboard rod, and M represents the torque applied by the flapping mechanism. During the modeling of the leading edge spar–spine system, θ_1 was assumed to be prescribed and it is expressed as shown in equation (4).

$$\theta_1 = \frac{\varphi}{2} \sin(\omega t) \quad (4)$$

where φ is the wing stroke angle, and ω is the flapping frequency in radians per second.

The EOM of the two rods shown in figure 6 were derived using Newton's principles and they are shown in equations (5) and (6).

$$I_1\ddot{\theta}_1 - k_T\left[\theta_2 - \theta_1\right] + m_2\ddot{y}_{2c.m.}L_1\cos\theta_1 - m_2\ddot{x}_{2c.m.}L_1\sin\theta_1 = M \quad (5)$$

$$I_2\ddot{\theta}_2 + k_T\left[\theta_2 - \theta_1\right] = 0 \quad (6)$$

where I_1 and I_2 are the mass moment of inertia of the inboard and outboard rods, respectively and $\ddot{x}_{2c.m.}$ and $\ddot{y}_{2c.m.}$ are the horizontal and vertical accelerations of the center of mass of the outboard rod, respectively.

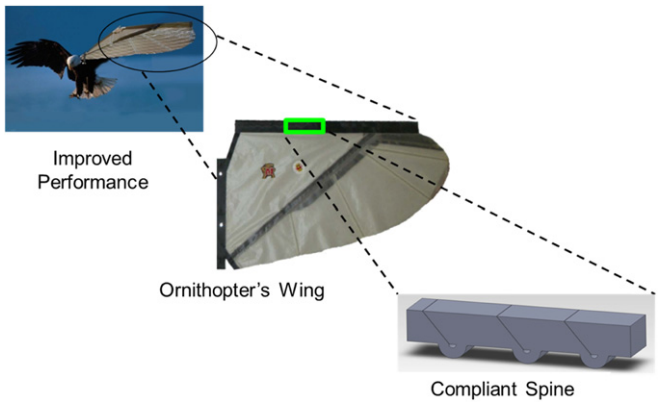

Figure 3. The compliant spine was inserted into the leading edge spar at 37% of the wing half span to mimic the function of an avian wrist.

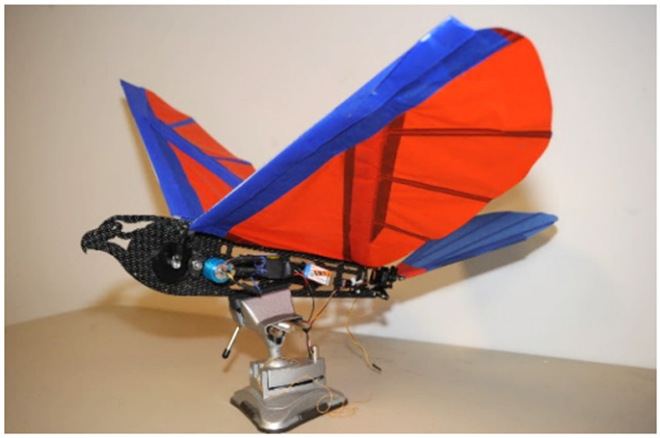

Figure 4. Test ornithopter.

Table 1. Test ornithopter specifications.

Specification	Value
Span	1.07 m
Flapping rate	4–6 Hz
Speed	2.5–8.5 m s^{-1}
Max. chord	0.28 m
Wing stroke angle	1.17 rad

Equations (5) and (6) are decoupled because the wing root angle was prescribed. Therefore, equation (6) can be solved directly for the spine root angle (θ_2). In the above model, equation (5) is considered a compatibility equation describing the amount of torque the flapping mechanism has to produce in order to drive the system at the prescribed wing root angle (θ_1). Matlab's® general forward time integration function, ODE45, was used to solve equation (6) numerically. The next section compares the analytically calculated wing root and spine root angles with their experimentally measured counterparts.

2.2. Experimental validation of leading edge spar

Constrained flight experimental data was used to validate the aforementioned model of the leading edge spar–spine system. Details about the experiment can be found in [16]. The experiment took place at NASA Langley Research Center (LaRC) thermal vacuum laboratory inside a 5 foot x 5 foot thermal vacuum chamber. The deflections of the leading edge spar were captured in order to measure the experimental wing root (θ_{1exp}) and spine root (θ_{2exp}) angles. Four retro-reflective markers were placed on the leading edge spar in order to capture its deflection. One marker was placed at the wing root, a second one was placed at the location of the compliant spine root, a third marker was placed at the location of the compliant spine tip, and a fourth marker was placed at the wing tip. The kinematics were captured using a Phantom V9.1 high-speed camera at 200 frames per second. The camera was mounted outside of the vacuum chamber as shown in figure 7(a). In order to illuminate the markers for tracking purposes, three LED light panels were mounted on the inside of the vacuum chamber as shown in figure 7(b). The analytical model described above did not include aerodynamic effects, thus in

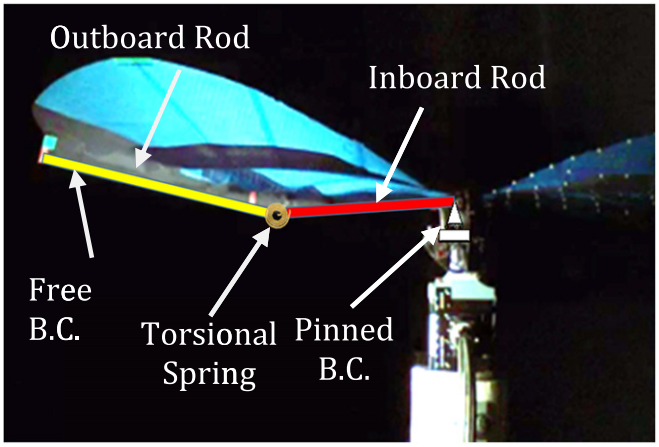

Figure 5. The research platform mounted on a test stand with the leading edge spar–spine model superimposed on the right wing for clarification.

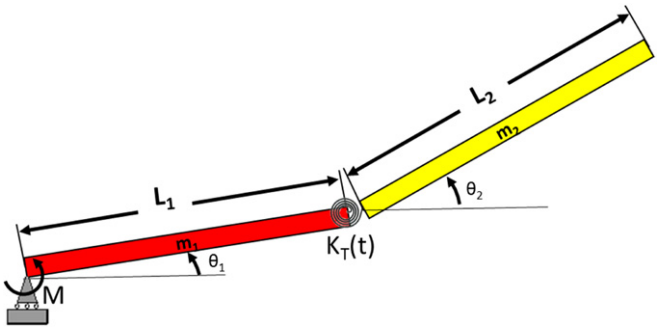

Figure 6. Detailed model of the leading edge spar with a torsional spring representing the compliant spine showing all relevant angles, lengths, and masses.

order to validate the model, an experimental setup where the effect of air is negligible was needed. Therefore, the experimental data used to validate the model was taken in rough vacuum at a pressure of 1 Torr.

The leading edge spar–spine configuration used to validate the model consisted of the leading edge carbon fiber spar with compliant spine design Comp 4TL inserted at 37% of the wing half span. Figure 8 shows an example of a wing spar–spine configuration. Figure 1 shows a schematic of compliant spine design, Comp 4TL. Comp 4TL has a mid-upstroke stiffness (k_u) of 3.75 N m rad^{-1} and a mid-downstroke stiffness (k_u) of 72.5 N m rad^{-1}. The mid upstroke and downstroke stiffness values were taken from a finite element analysis of the compliant spine under static and dynamic applied loads [5, 17]. During the experiment, the leading edge spar of the ornithopter was flapped at 4.2 Hz. This flapping frequency was selected because it is within the range of flapping frequencies suitable for free flight (see table 1). Figure 9 shows the leading edge spar–spine system bending deflection during the upstroke and downstroke under vacuum.

The wing root (θ_{1exp}) and spine root (θ_{2exp}) angles were calculated using the measured vertical displacement of the retro reflective markers as shown by equations (7) and (8).

$$\theta_{1\,\mathrm{exp}} = \sin^{-1}\frac{\left[Y_{SR} - Y_{WR}\right]}{L_1} \tag{7}$$

$$\theta_{2\,\mathrm{exp}} = \sin^{-1}\frac{\left[Y_{ST} - Y_{SR}\right]}{L_{spine}} \tag{8}$$

where Y_{WR}, Y_{SR}, and Y_{ST} are the vertical displacements of the wing root, spine root, and spine tip retro reflective markers respectively. L_{spine} is the compliant spine length, which was 6.35 cm (2.5″). Figure 10 and figure 11 compare the experimental data with the model results. The error between the experimental data and the model was calculated using equations (9) and (10).

$$\mathrm{RMSE}_{\theta_1} = \sqrt{\frac{\sum_1^n\left(\theta_{1\,\mathrm{exp}} - \theta_1\right)^2}{n}} \approx 7\,\% \tag{9}$$

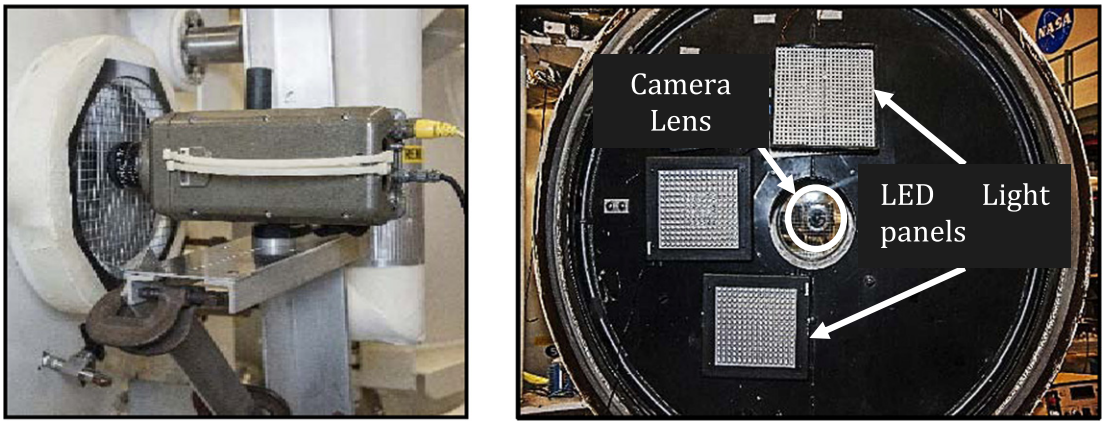

Figure 7. (a) A phantom high-speed camera mounted outside the vacuum chamber. (b) 3 LED panels mounted on the inside of the chamber to light the chamber and cause the markers to reflect light.

Figure 8. Example of a leading edge spar–spine configuration that was used to validate the leading edge spar analytical model.

$$\mathrm{RMSE}_{\theta_2} = \sqrt{\frac{\sum_1^n \left(\theta_{2\,\mathrm{exp}} - \theta_2\right)^2}{n}} \approx 11\ \% \qquad (10)$$

where n is the number of data points used over one flapping cycle.

The analytical wing root angle agrees within 7% of the experimental data while the analytical spine root angle agrees within 11% of the experimental data. The error observed in figure 10 and equation (9) are due to the assumption that the analytical wing root angle is sinusoidal. Experiments show that the wing root angle is not exactly sinusoidal. The wings spent more than half of the stroke below the horizontal plane. The error observed in figure 11 and equation (10) is attributed to the fact that any physical system has some structural damping, which was not accounted for in the model. Moreover, the model assumed that the carbon fiber spar was rigid while the physical carbon fiber spar had some flexibility. Finally the high frequency content noticed in the analytical spine root angle is typical for a bounded response of Mathieu's equation in which the ratio between the system's Eigen frequencies and frequency of excitation (flapping frequency) is small [18].

3. Leading edge spar stability analysis

3.1. Stability analysis via Strutt diagrams and phase plan plot

The structural stability of the leading edge spar–spine system can be determined using the experimentally validated analytical model. Equation (6) is written in the form of a non-homogeneous Mathieu's equation, as shown by equation (11). Equation (12) through (17) define the symbols in equation (11).

Several books and articles discuss the significance, history, and stability of Mathieu's equation [7, 19]. Mathieu's equation is very useful in the modeling of physical and mathematical systems. The solution of Mathieu's equation takes different forms and various levels of stability according to the values of the system parameters, δ and ϵ. Therefore it is necessary to determine the values of the δ and ϵ for which the leading edge spar–spine system may become unstable

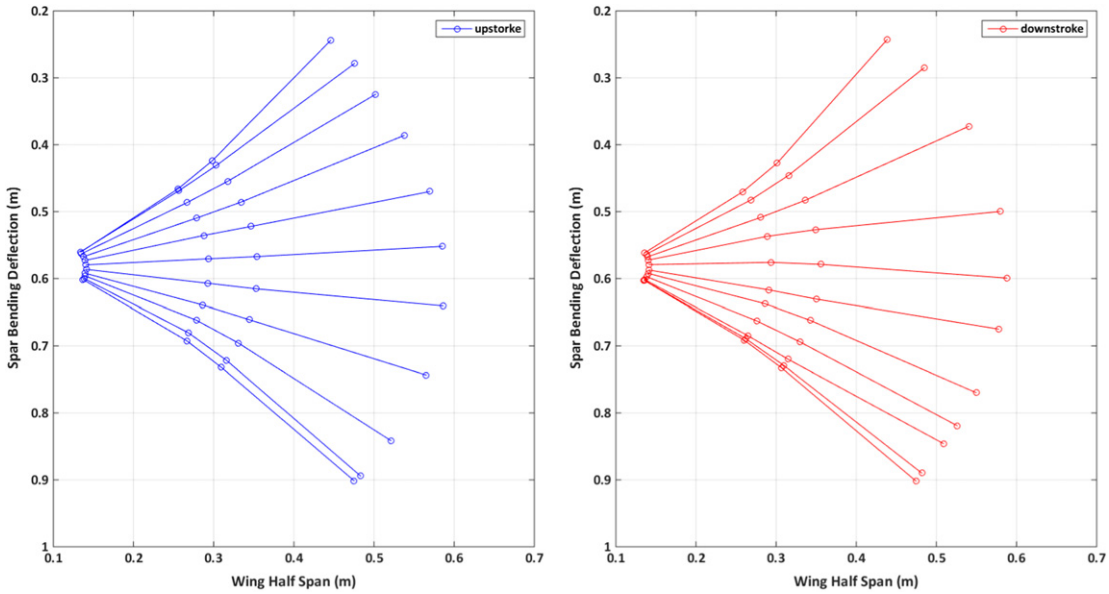

Figure 9. The bending deflection of the leading edge spar with Comp 4TL spine design inserted at 37% of the wing half span. These are the experimental deflections when the test platform was tested in rough vacuum at a pressure of 1 Torr.

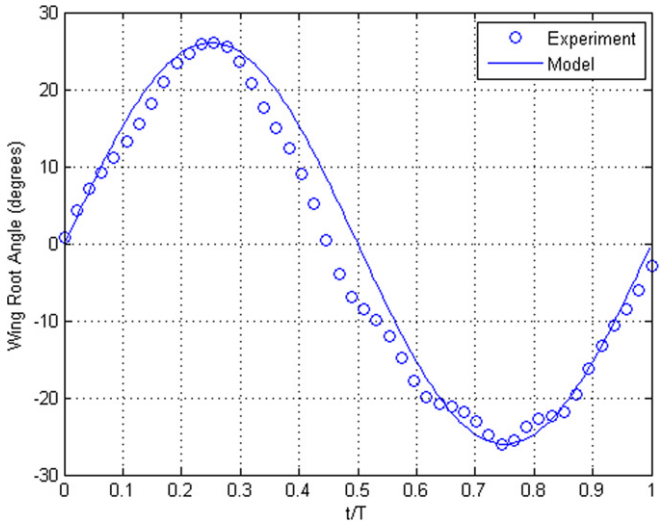

Figure 10. Experimental and analytical wing root angle versus time normalized by the period of one wing beat cycle. The experiment agrees with the model within 7%.

or have an unbounded response.

$$\ddot{\theta}_2(p) + [\delta + 2\epsilon \cos(2p)]\,\theta_2(p) = [\alpha + 2\beta \cos(2p)] \sin(2p) \tag{11}$$

$$\delta = \frac{k_a + k_b}{A} \tag{12}$$

$$\epsilon = \frac{-k_b}{2A} \tag{13}$$

$$\alpha = \frac{\varphi\left(k_a + k_b\right)}{2A} \tag{14}$$

$$\beta = \frac{-\varphi k_b}{4A} \tag{15}$$

$$p = \frac{\pi t}{T} \tag{16}$$

$$A = \frac{I_2 \pi^2}{T^2}. \tag{17}$$

The most common means of determining the stability of Mathieu's equation is using a Strutt diagram [20]. A Strutt diagram is a plot of the parameters δ versus ϵ. The lines shown in the diagram form boundaries between values of the parameters for which the solution is stable or unstable. The stability diagram was developed using the Hill's determinant method. Hill's determinant method was introduced in [21] and has been outlined in several publications since then [7, 20].

The stability of the leading edge spar–spine system can be determined using the Strutt diagram of the

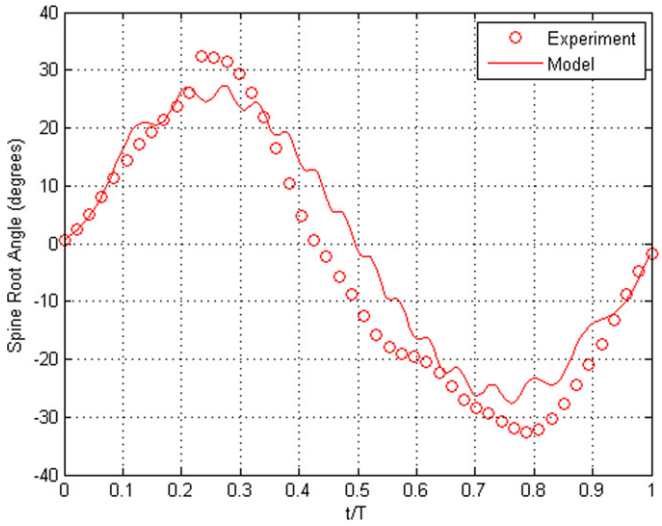

Figure 11. Experimental and analytical spine root angle versus time normalized by the period of one wing beat cycle. The experiment agrees with the model within 11%.

homogenous Mathieu's equation, equation (18). The non-homogeneous term on the right hand side of equation (11) does not affect stability because of the system's linearity.

$$\ddot{\theta}_2(p) + [\delta + 2\epsilon \cos(2p)]\,\theta_2(p) = 0. \tag{18}$$

Figure 12 shows the Strutt diagram of equation (18). The Strutt diagram is plotted in terms of δ and ϵ. Since the design parameters for the compliant spine are the upstroke and downstroke stiffness, it is useful to transform and plot the classical Strutt diagram in terms of the stiffness k_u and k_d. Figure 13 shows the transformed Strutt diagram. The figure also shows that design Comp 4TL, which is marked in the plot with the black dot, falls within a stable region of the Strutt diagram. Thus, the figure demonstrates that the leading edge spar–spine system, with design Comp 4TL inserted in it, is structurally stable.

The stability of equation (11) can also be shown analytically by solving for the system response and examining the phase plane plot. The phase plane is a plot of the system response (θ_2) versus its first derivative ($\dot{\theta}_2$). Figure 14 shows the phase plane plot of equation (11). The red dot in figure 14 signifies the initial conditions given to the system. The plot shows that the response of leading edge spar with design Comp 4TL inserted at 37% of the wing half span is bounded and stable.

3.2. Effect of damping on stability

The model discussed in section 2.1 did not include any damping. Any physical system includes some degree of damping known as structural damping. Moreover, aerodynamic loads on a flexible structure can be included in a system's EOM as an equivalent damping term. Thus, the inclusion of damping in the leading edge spar–spine model is important. In this section, the effect of adding damping on the structural stability of the leading edge spar–spine is investigated.

A viscous damper was added to the models of the leading edge spar–spine system as shown in figure 15. In the figure, C_T is the constant torsional damping coefficient in Newton meter seconds per radian. A linear damping model was assumed and the EOM of the outboard rod is expressed as shown in equation (19). Equations (20) and (21) defines the terms in equation (19). In equation (19), ζ is the damping ratio.

$$\ddot{\theta}_2(p) + 2\zeta\dot{\theta}_2(p) + [\delta + 2\epsilon \cos(2p)]\,\theta_2(p) = 2\gamma \cos(2p) + [\alpha + 2\beta \cos(2p)] \sin(2p) \tag{19}$$

$$\zeta = \frac{C_T T}{2\pi I_2} \tag{20}$$

$$\gamma = \frac{C_T T \varphi}{2\pi I_2}. \tag{21}$$

The structural stability of the leading edge spar with the torsional spring and damper was determined using the equation (22), which is the homogenous equation of equation (19). The non-homogeneous terms on the right hand side of equation (19) do not affect stability.

$$\ddot{\theta}_2(p) + 2\zeta\dot{\theta}_2(p) + [\delta + 2\epsilon \cos(2p)]\,\theta_2(p) = 0. \tag{22}$$

Equation (22) is known as the lossy Mathieu's equation and has been addressed frequently in the literature [7, 22]. The stability of equation (22) can also be determined using a Strutt diagram as shown by figure 16. Here the Strutt diagram is plotted in terms of δ and ϵ. The lines formed by the red markers are for the case of $\zeta = 0$. They are the same curves shown in figure 12. The lines formed by the blue and green markers are for the cases of $\zeta = 0.2$ and 0.5, respectively. The results in figure 16 confirm that adding

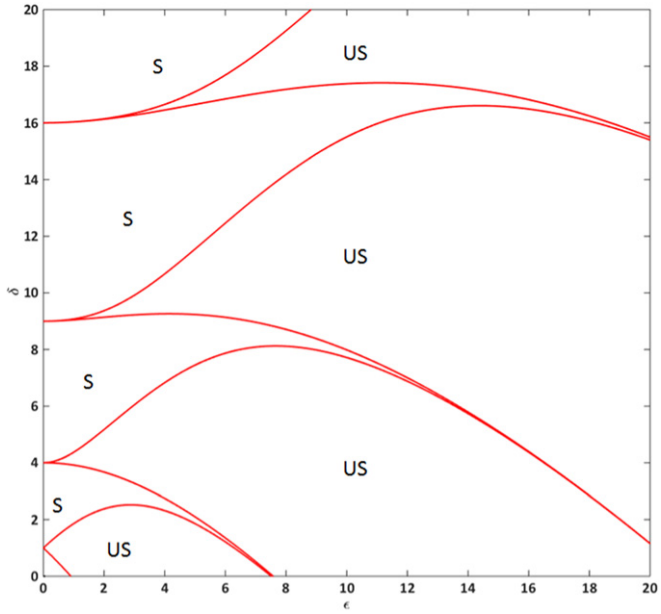

Figure 12. Strutt diagram for Mathieu's equation. The lines form boundaries or transition point between stable and unstable solution regions. Regions marked with US are unstable and regions marked with S are stable.

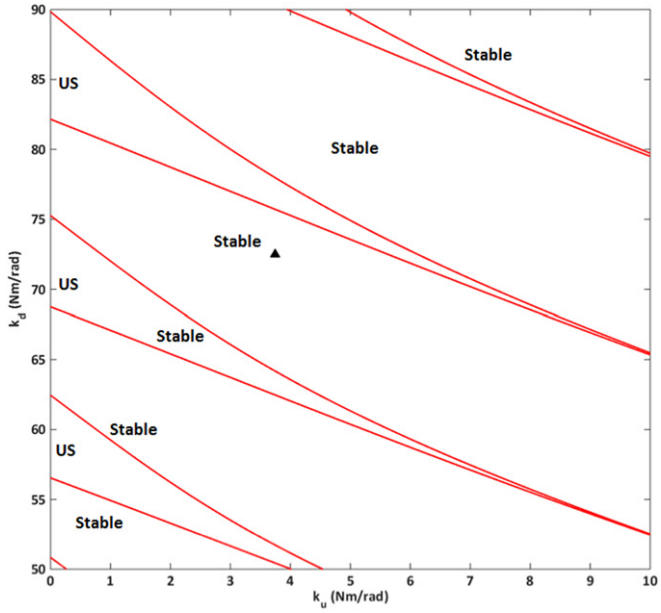

Figure 13. Strutt diagram for Mathieu's equation in terms of the upstroke and downstroke stiffness. The black marker represents compliant spine Comp 4TL. Regions marked with US are unstable regions.

damping has a stabilizing effect for $\zeta > 0$. The presence of damping shrinks the instability area. This figure was obtained by solving equation (22) numerically and using Floquet's theory to determine the stability criteria [20].

The design parameters for the compliant spine were the upstroke and downstroke stiffness, thus it is useful to transform and plot the classical Strutt diagram in terms of k_u and k_d to investigate the effect of damping on the design range for the up and down stroke stiffnesses. Figure 17 shows the transformed Strutt diagram. The results from the figure confirm that damping shrinks the instability regions, thus including viscous damping element into the leading edge spar–spine model is structurally stabilizing. More importantly, the figure shows that there exist a damping ratio between 0.2 and 0.5 for which areas of instability only occurs for $k_u < 0$. Given that the upstroke stiffness of the compliant spine is always greater than zero, it is concluded that there exists a value for ζ for which the leading edge spar is always stable regardless of the choice of upstroke and downstroke stiffness.

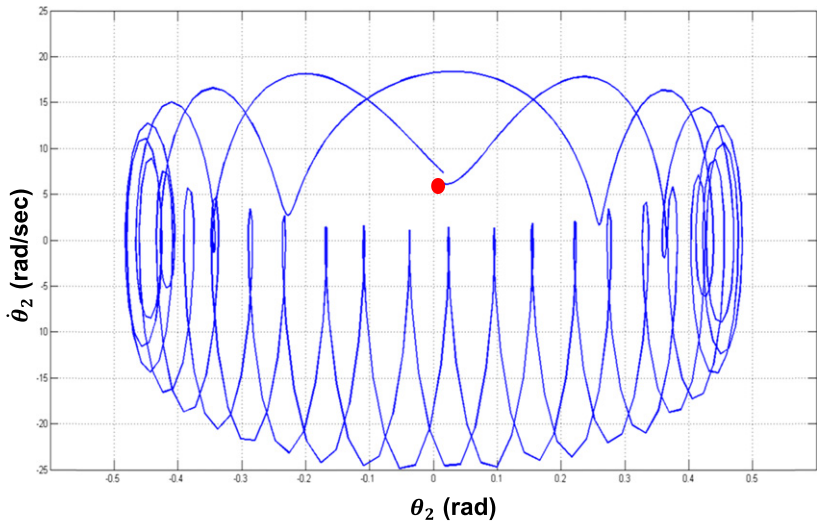

Figure 14. Phase plane plot of the spine root angle. The plot shows that the response of the leading edge spar with design Comp 4TL inserted at 37% of the wing half span is bounded and stable.

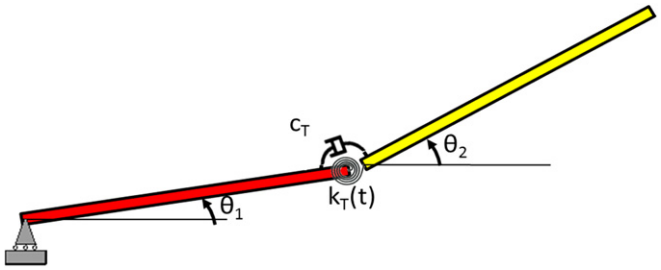

Figure 15. Model of the leading edge spar–spine system with a linear damping element.

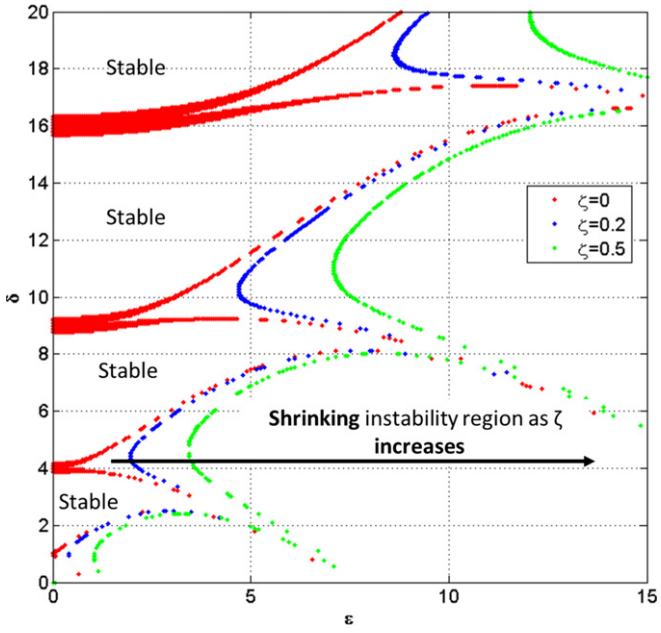

Figure 16. Strutt diagram of the Lossy Mathieu's equation for the cases of $\zeta = 0$ (red), 0.2 (blue), and 0.5 (green).

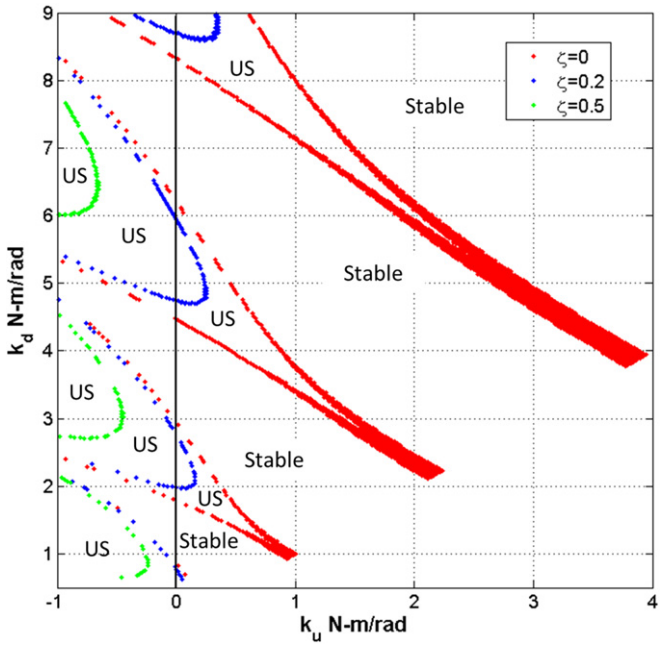

Figure 17. Strutt diagram for the Lossy Mathieu's equation in terms of the upstroke and downstroke stiffness for the cases of $\zeta = 0$ (red), 0.2 (blue), and 0.5 (green). Unstable regions shrink with increasing ζ and are marked by US.

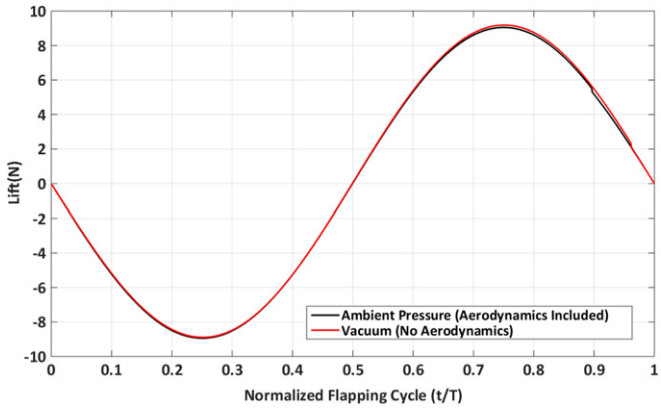

Figure 18. The lift produced by the leading edge spar–spine system over one flapping cycle and at a flapping frequency of 4.7 Hz both in ambient pressure and in vacuum. The figure shows that the inclusion of air does not affect the force produced over 1 flapping cycle.

3.3. The role of aerodynamics

The aerodynamic effects are not directly modeled in the aforementioned EOM but rather included implicitly in the damping term discussed in section 3.3. This approach is based on several conclusions made in previous related research efforts. Ellington [23] and Ennos [24] suggested that wing deformations are primarily due to inertial and elastic forces rather than aerodynamic forces. This suggestion have been confirmed even further during experiments and numerical analysis [25, 26] . Moreover, Combes and Daniel concluded that aerodynamics primarily provide damping to the wing structure, and the structural dynamics of the wing can be adequately calculated from a damped structural model without inclusion of aerodynamic terms [14, 26].

This paper focuses on determining the stability of a flapping wing vehicle leading edge spar with a variable stiffness compliant spine inserted in it. Given the small surface area of the spar–spine system, the forces due to aerodynamics are negligible when compared to the inertial forces. Therefore in the work presented in this paper, the effect of the aerodynamics on the wing deformation and forces produced by the leading edge spar is negligible. Figure 18 shows the lift produced by the leading edge spar–spine system over one flapping cycle and at a flapping frequency of 4.7 Hz both in ambient pressure and in vacuum. The figure shows

that the inclusion of air does not affect the force produced over 1 flapping cycle, thus confirming the conclusions made by previous work and the approach undertaken in this paper by including the aerodynamics through the damping term.

4. Conclusions

In this paper, the leading edge spar with an integrated variable stiffness compliant spine was modeled as a linear time periodic system. Such systems have a different stability criterion than that of a linear time invariant system. A stability analysis was necessary to ensure that the leading edge spar will remain structurally stable during testing. The EOM's of the leading edge spar–spine system were derived. The EOMs were solved numerically and the system's response was validated using experimental data. The experimental validation indicated that the modeled wing root and spine root angles agreed with the measured angles within 7% and 11%, respectively. The validated EOM, were then reformulated in terms of Mathieu's equation and the stability of the leading edge spar–spine system was determined both graphically and analytically. Stability was determined using a Strutt diagram that showed that the response of leading edge spar with a compliant spine design inserted at 37% of the wing half span was stable and bounded. Finally, the effect of damping on the structural stability of the leading edge spar was investigated. It was concluded that there exists a damping ratio for which the leading edge spar–spine system is stable for all values of compliant spine upstroke and downstroke stiffness.

Acknowledgments

The authors gratefully acknowledge the support of AFOSR grant number FA9550-09-1-0632 and FA9550-13-0126 under the direction of Dr David Stargel. The resources of NASA LaRC, the University of Maryland, the Pennsylvania State University, and the Morpheus Lab are also appreciated.

References

[1] Shyy W, Berg M and Ljungqvist D 1999 Flapping and flexible wings for biological and micro air vehicles *Prog. Aerosp. Sci.* **35** 455–506
[2] Tobalske B 2000 Biomechanics and physiology of gait selection in flying birds *Physiol. Biochem. Zool.* **73** 736–50
[3] Tobalske B and Dial K 1996 Flight kinematics of black-billed magpies and pigeons over a wide range of speeds *J. Exp. Biol.* **199** 263–80 (http://jeb.biologists.org/content/jexbio/199/2/263.full.pdf)
[4] Tobalske B 2007 Biomechanics of bird flight *J. Exp. Biol.* **210** 3135–46
[5] Tummala Y, Wissa A, Frecker M and Hubbard J Jr 2014 Design and optimization of a contact-aided compliant mechanism for passive bending *J. Mech. Robot.* **6** 031013
[6] Wissa A, Tummala Y, Hubbard J Jr and Frecker M 2012 Passively morphing ornithopter wings using a novel compliant spine: design and testing *Smart Mater. Struct.* **21** 094028
[7] Wereley N M 1991 *Analysis and Control of Linear Periodically Time Varying Systems* (Cambridge, MA: Massachusetts Institute of Technology)
[8] Butikov E I 2004 Paramteric excitation of a linear oscillator *Eur. J. Phys.* **25** 535–54
[9] Harmon R 2006 Aerodynamic modeling of flapping membrane wing using motion tracking experiments *Master's Thesis* University of Maryland
[10] Orlowski C and Girard A 2012 Dynamics, stability, and control analyses of flapping wing micro-air vehicles *Prog. Aerosp. Sci.* **51** 18–30
[11] Stanford B and Beran P 2013 Optimal flapping-wing vehicle dynamics via Floquet mulitplier sensitivities *J. Guid. Control Dyn.* **36** 455–66
[12] Wu J H and Sun M 2012 Floquet Stability analysis of the longitudinal dynamics of two hovering model insects *J. R. Soc.* **9** 2033–46
[13] Su W and Cesnik C 2011 Flight dynamic stability of a flapping wing micro air vehicle in hover *52nd AIAA/ASME/ASCE/AHS/ASC Structures, Structural Dynamics and Materials Conf.* (*Denver*)
[14] Rosenfield N and Wereley N 2009 Time-periodic stability of a flapping insect wing structure in hover *J. Aircr.* **46** 450–65
[15] Wissa A, Grauer J, Guerreiro N, Roberts R, Altenbuchner C, Hubbard J Jr, Tummala Y and Frecker M 2013 Flight testing of novel compliant spines for passive wing morphing on ornithopters *54TH AIAA/ASME/ASCE/AHS/ASC Structures, Structural Dynamics, and Materials Conf.* (*Boston*)
[16] Wissa A, Tummala Y, Hubbard J Jr, Frecker M and Northrup M 2014 Inertial effects due to passive wing morphing in ornithopters *22nd AIAA/ASME/AHS Adaptive Structures Conf.* (*National Harbor*)
[17] Tummala Y, Wissa A, Frecker M and Hubbard J Jr 2010 Design of a passively morphing ornithoper wing using a novel compliant spine *Conf. Smart Materials, Adaptive Structures and Intelligent Systems* (*Philadelphia*) pp 703–13
[18] Nayfeh A 1979 *Nonlinear Oscillations* (New York: Wiley)
[19] McLachlan N W 1964 Theory and application of mathieu functions (New York: Dover)
[20] Simakhina S V 2003 Stability analysis of Hill's equation *PhD Thesis* University of Illinois-Chicago
[21] Hill G W 1886 On the part of the lunar perigree which is a function of the mean motions of the Sun and the Moon *Acta Math.* **8** 1–36
[22] Richards J A 1976 Stability diagram approximation for the lossy mathieu equation *SIAM J. Appl. Math.* **30** 240–7
[23] Ellington C 1984 The aerodynamics of hovering insect flight: VI. Lift and power requirements *Phil. Trans. R. Soc.* B **305** 145–81
[24] Ennos A 1989 Inertial and aerodynamic torques on the wings of diptera in flight *J. Exp. Biol.* **142** 87–95 (http://jeb.biologists.org/content/142/1/87.short)
[25] Singh B and Chopra I 2008 Insect-based hover-capable flapping wings for micro air vehicles: experiments and analysis *AIAA J.* **46** 2115–35
[26] Combes S and Daniel T 2003 Into thin air: contributions of aerodynamic and inertial-elastic forces to wing bending in the hawkmoth manduca sexta *J. Exp. Biol.* **206** 2999–3006